Robustness of the ePIE algorithm for the complete characterization of femtosecond, extreme ultra-violet pulses

MARIO MURARI,[1,2] **GIACINTO D. LUCARELLI,**[1,2] **MATTEO LUCCHINI,**[1,2] (iD) **AND MAURO NISOLI**[1,2,*] (iD)

[1]*Department of Physics, Politecnico di Milano, 20133 Milano, Italy*
[2]*Institute for Photonics and Nanotechnologies, IFN-CNR, 20133 Milano, Italy*
*mauro.nisoli@polimi.it

Abstract: Frequency-resolved optical gating for the complete reconstruction of attosecond bursts (FROG-CRAB) is a well-known technique for the complete temporal characterization of ultrashort extreme ultraviolet (XUV) pulses, with durations down to a few tens of attoseconds. Recently, this technique was extended to few-femtosecond XUV pulses, produced by high-order harmonic generation (HHG) in gases, thanks to the implementation of a robust iterative algorithm: the extended ptychographic iterative engine (ePIE). We demonstrate, by using numerical simulations, that the ptychographic reconstruction technique is characterized by an excellent degree of convergence and robustness. We analyse the effects on pulse reconstruction of various experimental imperfections, namely, the jitter of the relative temporal delay between the XUV pulse and a suitably delayed infrared (IR) pulse and the noise of the measured FROG-CRAB spectrograms. We also show that the ePIE approach is particularly suitable for the reconstruction of incomplete FROG-CRAB spectrograms (i.e., spectrograms with a reduced number of measured time delays) and of spectrograms acquired with a reduced spectral resolution, particularly when relatively high-intensity IR pulses are employed.

1. Introduction

Few-femtosecond extreme-ultraviolet (XUV) pulses are important tools for the investigation of ultrafast dynamics of core and deep valence levels in molecules and solids [1–4]. High-order harmonic generation (HHG) in gases is the method routinely used for the production of ultrashort XUV pulses with duration ranging from a few tens of femtoseconds to a few tens of attoseconds [5]. Femtosecond pulses tunable in a broad spectral region can be produced by spectral selection of individual harmonic orders. The use of a time-delay compensated monochromator (TDCM) is particularly useful, since it allows the selection of single harmonic peaks preserving the temporal duration of the corresponding XUV pulses [6–9]. Recently, the generation and complete temporal characterization of XUV pulses spectrally selected by employing a TDCM, with duration down to 5 fs, has been reported [10]. Complete and accurate characterization of the temporal and spectral characteristics of the XUV pulses can be crucial for a correct analysis of the results of time-resolved experiments based on them. Frequency-resolved optical gating for the complete reconstruction of attosecond bursts (FROG-CRAB) [11] is becoming the method of choice for the characterization of ultrashort XUV pulses, in particular in the case of isolated attosecond pulses [12,13]. In a FROG-CRAB measurement an XUV pulse photoionizes atoms in the presence of an infrared (IR) laser field [14]. The energy spectra of the photoelectrons are then measured as a function of the temporal delay between the XUV and IR pulses thus obtaining a spectrogram, which contains all the information about the temporal characteristics of the pulse. The application of the FROG-CRAB technique to femtosecond XUV pulses is not trivial, due to the reduction of information redundancy in the case of femtosecond pulses, which are

characterized by relatively narrow bandwidths. As demonstrated by Lucchini *et al.* [10], an accurate reconstruction of the temporal amplitude and phase of single harmonics can be achieved with the FROG-CRAB technique when combined with a robust iterative algorithm as the extended ptychographic iterative engine (ePIE), which is characterized by superior degree of convergence and robustness [10,15–17]. Ptychography is a coherent diffraction imaging technique, with interesting applications in optical microscopy in the visible, XUV and X-ray spectral regions [18]. The first time-domain ptychography was introduced by Spangenberg *et al.* in 2015 [19].

Here we show, with numerical simulations, that the ePIE technique is a particularly powerful approach to achieve complete reconstruction of the temporal characteristics of single harmonic pulses. The aim of the work is to investigate the robustness of the ePIE method against unavoidable experimental imperfections, which may introduce uncertainties in the reconstruction of the XUV pulses. Various sources of experimental imperfections will be considered. In particular, the effects on pulse reconstruction of a time jitter of the relative temporal delay between XUV and IR pulses will be investigated in Sec. 3.1. The effects of noise on the measured FROG-CRAB spectrograms, which limit the achievable signal-to-noise ratio, will be analysed in Sec. 3.2. Robustness of the ePIE method applied to spectrograms obtained by reducing the number of delay steps will be discussed in Sec. 4. We will demonstrate that, similarly to what already observed in the application of ptychographic reconstruction algorithm to FROG traces [17], the temporal characteristics of femtosecond XUV pulses can be well reconstructed even when the temporal axis of the FROG-CRAB spectrogram in strongly under-sampled. This is particularly important for the applications since a reduction of the delay steps required for an accurate reconstruction of the XUV pulses corresponds to a reduction of the acquisition time. The effects of the limited bandwidth of the experimental apparatus used for the FROG-CRAB measurement will be studied in Sec. 5. Temporal characterization of XUV pulses with photon energies close to the ionization potential of the gas used for the FROG-CRAB measurement will be discussed in Sec. 6.

2. FROG-CRAB spectrograms: simulation parameters

In the following we will employ the ePIE algorithm to reconstruct the temporal and spectral characteristics of femtosecond XUV pulses starting from the measurement of FROG-CRAB spectrograms, given by (atomic units are used) [20]

$$S(\mathbf{p}, \tau) = \left| \int dt \, \mathbf{E}_{XUV}(t - \tau) \cdot \mathbf{d}[\mathbf{p} + \mathbf{A}_{IR}(t)] \, e^{-i\phi(\mathbf{p},t)} \, e^{i(\frac{p^2}{2} + I_p)t} \right|^2, \tag{1}$$

where

$$\phi(\mathbf{p}, t) = \int_t^\infty dt' \left(\mathbf{p}\mathbf{A}_{IR}(t') + \frac{A_{IR}^2(t')}{2} \right). \tag{2}$$

I_p is the ionization potential of the photoionized gas, $\mathbf{p}$ is the electron momentum, $\mathbf{E}_{XUV}(t)$ is the electric field of the XUV pulse, $\mathbf{A}_{IR}(t)$ is the vector potential of the IR pulse, $\mathbf{d}$ is the atomic dipole, τ is the temporal delay between XUV and IR pulses. In the framework of the central momentum approximation (CMA), Eq. (1) can be factorized as an internal product between a pulse function $P(t)$ and a gate function $G(t)$, which depends only on time, so that the spectrogram of Eq. (1) can be written as

$$S(\mathbf{p}, \tau) = \left| \int dt \, P(t - \tau)G(t) \, e^{i(\frac{p^2}{2} + I_p)t} \right|^2, \tag{3}$$

where

$$P(t) = \mathbf{E}_{XUV}(t) \cdot \mathbf{d}[\mathbf{p}_c + \mathbf{A}_{IR}(t)], \tag{4}$$

$\mathbf{p}_c$ is the central electron momentum and $\mathbf{d}$ is assumed constant. The pure phase gate function $G(t)$ is given by

$$G(t) = e^{-i\phi(\mathbf{p}_c, t)} \tag{5}$$

In the simulations the electric field envelopes of the IR and XUV pulses were assumed to be Gaussians:

$$E(t) = E_0 \exp(-t^2/2\sigma^2)\sin(\omega_0 t) \tag{6}$$

where ω_0 is the central angular frequency ($\omega_0 = \omega_{IR}$ for the IR field, $\omega_0 = \omega_{XUV}$ for the XUV field). The temporal width σ is related to the intensity full-width half maximum (FWHM) duration, Δt, by $\sigma = \Delta t/2\sqrt{\ln 2}$. Realistic pulse parameters were considered. Transform-limited IR pulses were assumed with a FWHM duration $\Delta t_{IR} = 10$ fs and central wavelength of 800 nm. In the following sections, except when differently stated, the 27-th harmonic (H27) will be considered, with a bandwidth corresponding to a transform-limited duration $\Delta t_{H27} = 5$ fs, to reproduce the experimental conditions [10]. A quadratic spectral phase term was added in the case of XUV pulses by multiplying the field Fourier transform by $\exp[iD_2(\omega - \omega_{XUV})^2/2]$, where D_2 is the group delay dispersion (GDD). In the simulations we chose argon as a target gas for the FROG-CRAB measurements (ionization potential $I_p = 15.76$ eV). We assumed a constant cross-section for Argon on the bandwidth of the considered harmonics. In all the ePIE reconstructions presented here, the spectrograms were sampled to 512 points in energy (energy step $\Delta E = 23.4$ meV) and 41 points in temporal delay (delay step $\Delta \tau = 2$ fs). All spectrograms were normalized to one, i.e. the maximum of the XUV-only photoelectron spectrum equals 1. In the following section various sources of experimental imperfections will be analysed, which may lead to an incorrect reconstruction of the XUV and IR temporal characteristics. In this work, we will not investigate the effect of pulse-to-pulse instabilities, i.e., we will not consider situations where the pulse intensity or phase varies on a time scale shorter than the measurement time. In this case, multi-shot pulse-measurement techniques usually exhibit a coherent artifact, which substantially complicates the interpretation of the measurement [21,22]. The analysis of this effect goes beyond the scope of our work and would require a different approach, as reported by Bourassin-Bouchet and co-workers [23].

3. Effects of experimental imperfections on ePIE reconstructions

3.1. Effects of temporal jitter

We have first analysed the effects on pulse reconstruction of a temporal jitter of the time delay between the IR and XUV pulses, induced, for instance, by small variations of the IR and XUV beam-paths during the acquisition of the FROG-CRAB traces. In the simulations the temporal jitter was assumed to randomly change around the nominal value of the XUV-IR delay with a Gaussian distribution. The corresponding spectrogram can be written as follows:

$$S_J(\omega, \tau) = \sum_{\tau_J} S(\omega, \tau - \tau_J) \exp\left[-\frac{(\tau - \tau_J)^2}{\Delta t_J^2}8\ln 2\right] \tag{7}$$

where τ_J is a given jitter value and Δt_J is the FWHM of the Gaussian time-jitter distribution. A series of spectrograms, $S_J(\omega, \tau)$, was calculated by varying Δt_J from 0 to 5 fs.

Figure 1(a) shows the spectrogram calculated in the case of H27 assuming a temporal jitter with $\Delta \tau_J = 5$ fs and considering an IR intensity $I_{IR} = 1 \times 10^{11}$ W/cm^2. Figure 1(b) displays the reconstructed spectrogram. The solid blue and green curves in Fig. 1(c) correspond to the theoretical spectral amplitude and phase, respectively, of the XUV pulse. The blue and green circles represent the results of the reconstruction. Figure 1(d) shows the input (solid curve) and the reconstructed (circles) temporal intensity profile of the IR pulse. As clearly evidenced by the
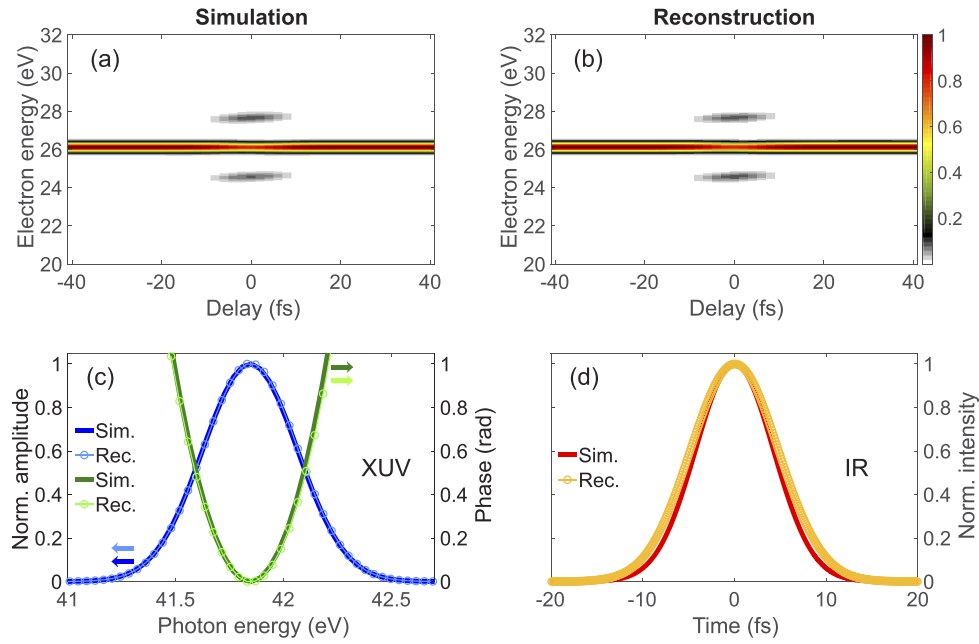
Fig. 1. Effects of a temporal jitter (with $\Delta t_J = 5$ fs) between XUV and IR pulses on ePIE reconstruction for harmonic H27, assuming an XUV pulse with FWHM-duration $\Delta t_{XUV} = 6.33$ fs ($D_2 = 7$ fs^2) and a transform-limited, 10-fs, IR pulse with intensity $I_{IR} = 1 \times 10^{11}$ W/cm^2. Simulated (a) and reconstructed (b) spectrograms. (c) Simulated (solid lines) and reconstructed (circles) XUV spectral amplitude and phase. (d) Simulated (solid line) and reconstructed (circles) IR temporal intensity profile.

results reported in Fig. 1, the temporal and spectral characteristics of the XUV pulses are well reconstructed, despite the notable time jitter considered in the simulations.

The modifications of the retrieved XUV pulse duration (FWHM) upon increasing the time jitter from 0 to 5 fs is shown in Fig. 2(a) for two different IR intensities, generating a single sideband ($I_{IR} = 1 \times 10^{11}$ W/cm^2) or multiple sidebands ($I_{IR} = 1 \times 10^{12}$ W/cm^2). At the lowest IR intensity
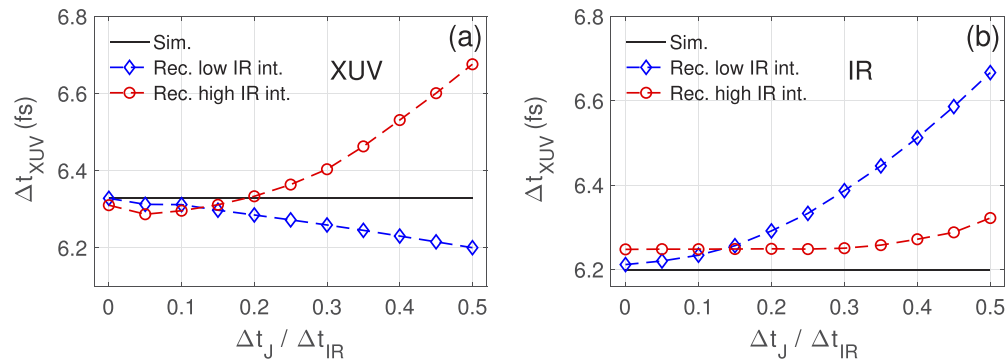

Fig. 2. Comparison of simulated and reconstructed XUV (a) and IR (b) pulse durations as a function of the ratio between the temporal jitter and the FWHM-duration of the IR pulse, for two IR intensities (blue diamonds: $I_{IR} = 1 \times 10^{11}$ W/cm^2; red circles: $I_{IR} = 1 \times 10^{12}$ W/cm^2). XUV and IR pulses with the same parameters of Fig. 1.

the reconstructed duration slightly decreases upon increasing the jitter, with a maximum relative variation of ∼ 2%. At the highest IR intensity the reconstructed duration increases with jitter, with a maximum relative increase of ∼ 6%. The reconstructed duration of the IR pulse, shown in Fig. 2(b), increases with jitter for both values of the IR intensity, with a maximum relative variation of ∼ 12% at the lowest intensity. Therefore, the generation of multiple sidebands does not increase the accuracy of the XUV pulse reconstruction, while it favours a better reconstruction of the IR pulse.

3.2. Effects of noise

From the experimental point of view spectrograms always contain noise. Signal-to-noise ratio can be optimized for example by increasing the number of acquired electrons per pump-probe delay, thus increasing the total acquisition time. A compromise between acquisition time and accuracy of the XUV pulse characterization must be achieved. In this section the effect of noise on the measured spectrograms and the robustness of ePIE algorithm will be analysed. For each pixel of the two-dimensional map which represents the spectrogram we have assumed a Gaussian white noise distribution, characterized by a variance, σ_n^2, proportional to the pixel intensity as follows

$$\sigma_n^2 = \beta S_0(\omega, \tau) \tag{8}$$

where $S_0(\omega, \tau)$ is the simulated spectrogram without noise and β is a proportionality factor (noise factor) ranging from 0.02 to 0.2. A locally variable noise is considered to mimic the experimental data, which display a noise proportional to the signal. Figures 3(a) and 4(a) show
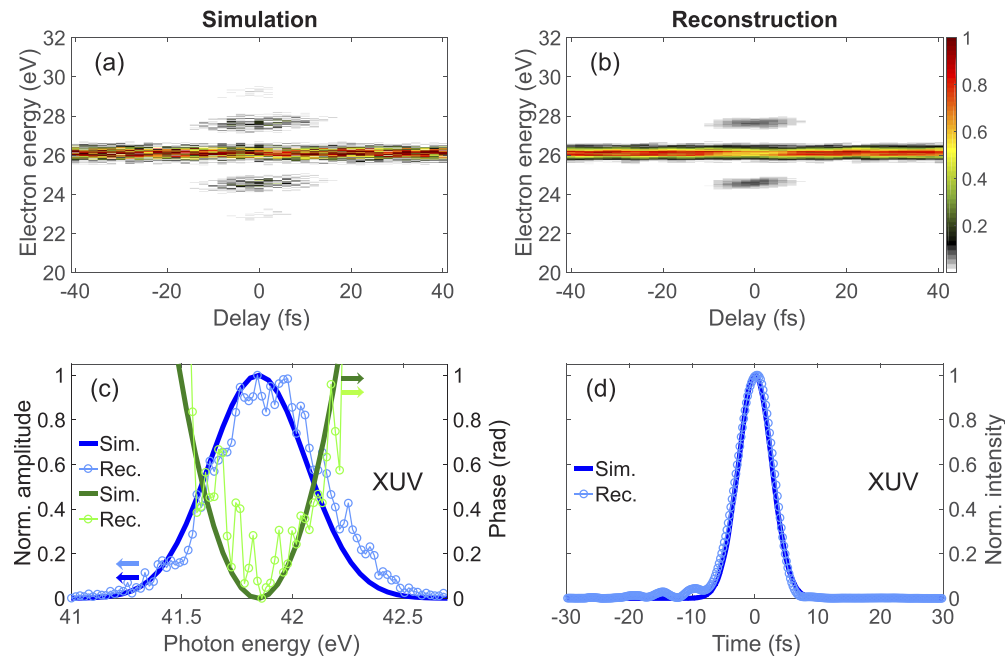

Fig. 3. Effects of noise on ePIE reconstruction for harmonic H27, assuming an XUV pulse with FWHM-duration $\Delta t_{XUV} = 6.33$ fs ($D_2 = 7$ fs^2), a transform-limited IR pulse with intensity $I_{IR} = 1 \times 10^{11}$ W/cm^2 and a noise factor $\beta = 0.2$. Simulated (a) and reconstructed (b) spectrograms. (c) Simulated (solid lines) and reconstructed (circles) XUV spectral amplitude and phase. (d) Simulated (solid line) and reconstructed (circles) XUV temporal intensity profile.

the spectrograms calculated for two values of the IR pulse intensity, assuming a Gaussian white noise with $\beta = 0.2$. Figures 3(b) and 4(b) show the reconstructed spectrograms. The simulated and reconstructed XUV spectral amplitude and phase are shown in Figs. 3(c) and 4(c), while simulated and reconstructed XUV intensity profiles are displayed in Figs. 3(d) and 4(d). Despite the large value of the noise factor assumed for these simulations, the spectral and temporal characteristics of the XUV pulses are reasonably well reproduced, in particular when multiple sidebands are present. On the contrary, the quality of the reconstruction of the IR pulse, not shown in Figs. 3–4, is rather poor: only the FWHM duration is roughly reproduced. The fact that the ePIE algorithm favours the XUV pulse reconstruction in spite of the IR pulse was already observed in [24].

In order to quantitatively estimate the quality of the XUV spectrogram reconstruction, an error function, ξ, is calculated as an rms average across the entire trace of the difference between the reconstructed, $S_R(\omega, \tau)$, and simulated, $S_S(\omega, \tau)$, spectrograms [25]:

$$\xi = \min_\alpha \left\{ \sum_{\omega, \tau} \frac{\sqrt{[S_R(\omega, \tau) - \alpha S_S(\omega, \tau)]^2}}{N_{th}} \right\} \tag{9}$$

where: α is a scaling parameter, ω is the angular frequency, τ is the XUV-IR relative time delay and N_{th} is the number of points of the simulated trace having more electron counts than a thousandth of the maximum collected electrons per point. The error ξ is minimized with respect to α on each iteration.
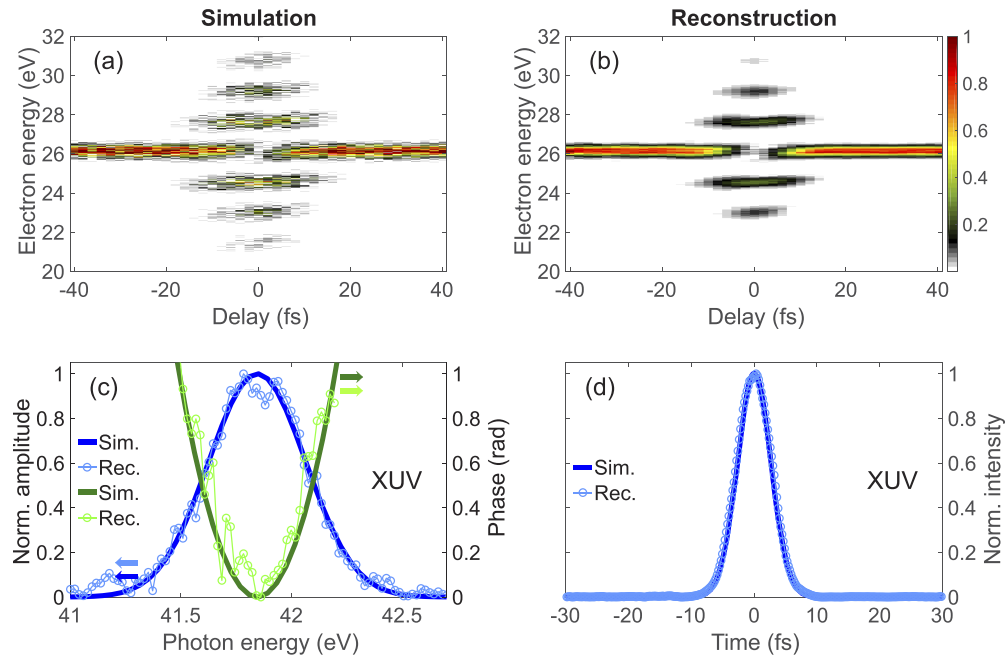

Fig. 4. Effects of noise on ePIE reconstruction. Same parameters as in Fig. 3 but assuming an IR intensity $I_{IR} = 1 \times 10^{12}$ W/cm^2.

Figure 5(a) shows the reconstructed XUV pulse duration (FWHM) as a function of the noise factor in the case of single sideband generation (low intensity) and multiple sideband generation (high intensity). 30 simulations were performed for each value of β, each one with a different noise pattern. The error bars give the standard deviation of the reconstructed pulse duration for each β

value. In the case of single sideband generation, while the average value of the reconstructed pulse duration does not appreciably change with the noise level and nicely reproduces the correct value, the standard deviation significantly increases with noise level. Furthermore, the accuracy of the XUV pulse reconstruction improves by increasing the IR pulse intensity, as indicated by the reduction of the amplitude of the error bars. This is clearly shown in Fig. 5(b), which displays
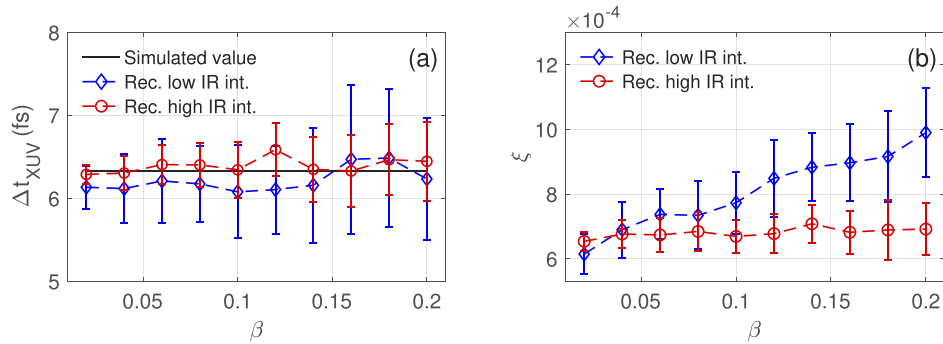

Fig. 5. (a) Reconstructed temporal duration of the XUV pulse as a function of the noise factor β, for two different IR intensities. Low intensity: $I_{IR} = 1 \times 10^{11}$ W/cm^2; high intensity: $I_{IR} = 1 \times 10^{12}$ W/cm^2. (b) Reconstruction error, ξ (see Eq. (9) in the text), as a function of the noise factor β.
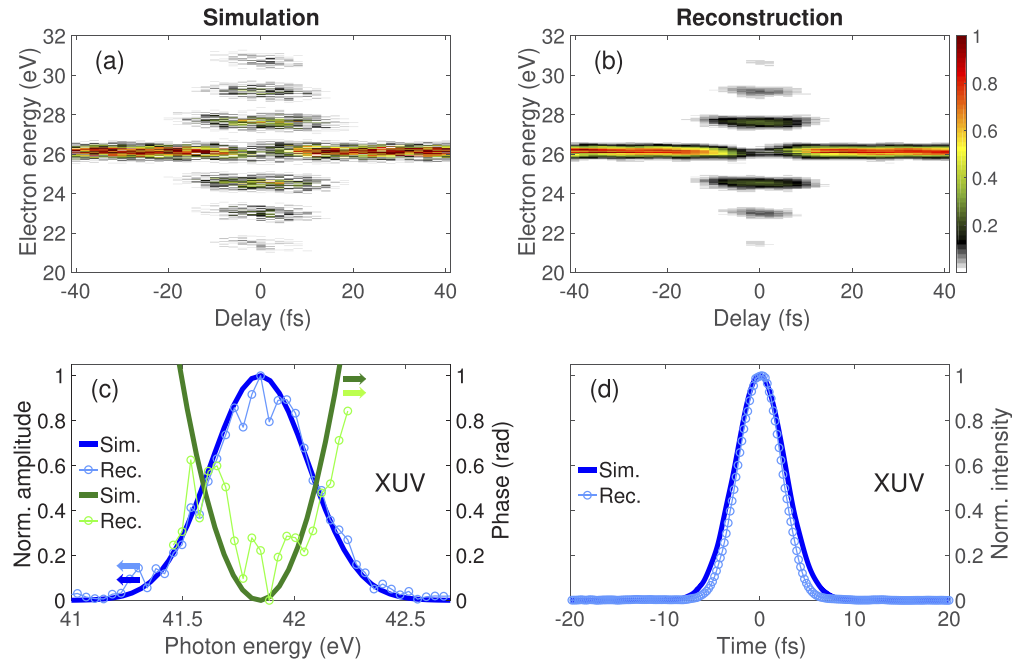

Fig. 6. Effects of a temporal jitter (with $\Delta t_J = 5$ fs) between XUV and IR pulses and of noise (noise factor $\beta = 0.2$) on ePIE reconstruction for harmonic H27, assuming an XUV pulse with FWHM-duration $\Delta t_{XUV} = 6.33$ fs ($D_2 = 7$ fs^2) and a transform-limited, 10-fs, IR pulse with intensity $I_{IR} = 1 \times 10^{12}$ W/cm^2. Simulated (a) and reconstructed (b) spectrograms. (c) Simulated (solid lines) and reconstructed (circles) XUV spectral amplitude and phase. (d) Simulated (solid line) and reconstructed (circles) XUV temporal intensity profile.

the error function ξ as a function of the noise factor. A low and almost constant ξ is achieved at high IR intensity, while the reconstruction error increases upon an increasing noise when a single sideband is generated. As a general conclusion, when the experimental measurement is affected by a relatively high level of noise, it is useful to increase the IR pulse intensity in order to generate multiple sidebands.

We have then considered the reconstruction of XUV pulses under the effect of both time jitter and noise. As a particular example, we have assumed a temporal jitter with $\Delta t_J = 5$ fs and a Gaussian white noise with $\beta = 0.2$. Figure 6(a) shows the spectrogram generated by H27, with FWHM-duration $\Delta t_{XUV} = 6.33$ fs ($D_2 = 7$ fs^2) and an IR pulse having enough intensity to be in the multiple-sideband regime ($I_{IR} = 1 \times 10^{12}$ W/cm^2). The associated reconstructed spectrogram is displayed in Fig. 6(b). The solid blue and green curves in Fig. 6(c) correspond to the theoretical spectral amplitude and phase, respectively, of the XUV pulse. The blue and green circles represent the results of the reconstruction. Figure 6(d) shows the input (solid curve) and the reconstructed (circles) temporal intensity profile of the XUV pulse. Clearly, the temporal and spectral characteristics of the XUV pulses are well reconstructed, despite the notable time jitter and noise level considered in the simulations. On the contrary, the IR pulse was not properly reconstructed.

4. ePIE reconstruction of incomplete spectrograms

It is well known that a complete FROG trace is greatly redundant [25]; while the pulse is represented by a vector composed by N complex values, the corresponding FROG trace is composed by N^2 pixels. As pointed out in Ref. [17], the use of the ptychographic technique
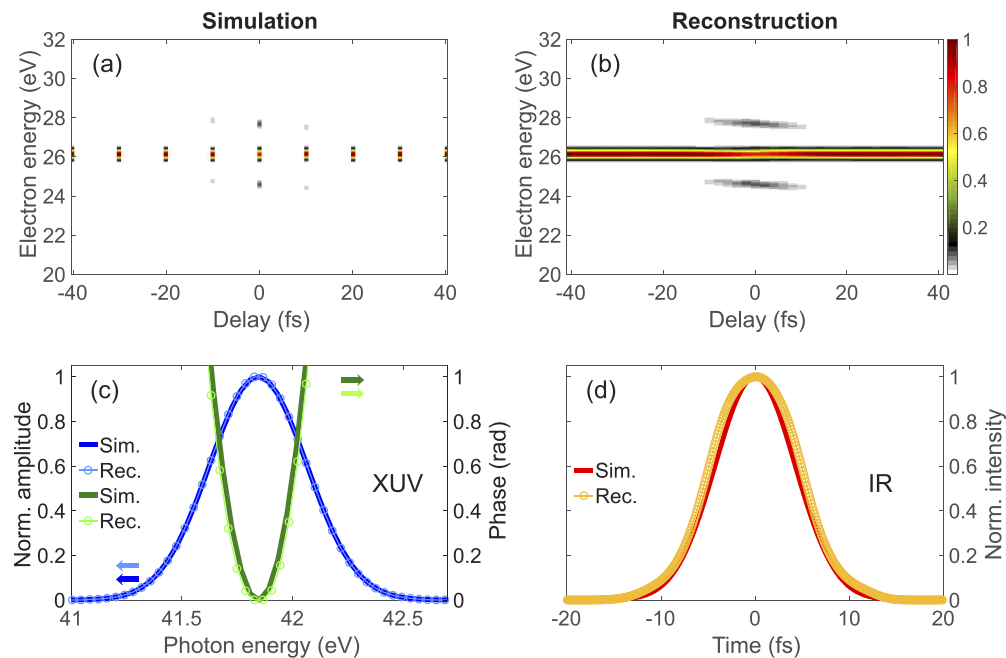

Fig. 7. Reconstruction of incomplete spectrograms in the case of harmonic H27 with $\Delta t_{XUV} = 12.17$ fs ($D_2 = 20$ fs^2) and a transform-limited, 10-fs, IR pulse with intensity $I_{IR} = 1 \times 10^{11}$ W/cm^2, assuming $\eta = 0.822$. Simulated (a) and reconstructed (b) spectrograms. (c) Simulated (solid lines) and reconstructed (circles) XUV spectral amplitude and phase. (d) Simulated (solid line) and reconstructed (circles) IR temporal intensity profile.

enables the reconstruction of pulses starting from significantly incomplete FROG traces, i.e., from spectrograms with a reduced number of measured time delays. This originates from the fact that in the ptychographic approach the delay and energy axes are completely uncoupled. Moreover, this reconstruction technique is sensitive to the absolute value of the delay and not only to the relative step size, so that the delay steps do not need to be constant. The choice of the step size is related to the temporal characteristics of the pulses. We define a parameter η as the ratio between the step size and the FWHM-duration of the XUV pulse.

Figure 7(a) shows the spectrogram calculated for the harmonic H27, with a relatively strong chirp, $D_2 = 20$ fs^2, (FWHM-duration $\Delta t_{XUV} = 12.17$ fs) and a transform-limited, 10-fs, IR pulse with intensity $I_{IR} = 1 \times 10^{11}$ W/cm^2, assuming $\eta = 0.822$. The spectrogram reconstructed (extrapolated) after the application of the ePIE algorithm is shown in Fig. 7(b). Spectral intensity profile and phase of the reconstructed XUV pulse are reported in Fig. 7(c), together with the original pulse spectral characteristics, while the temporal intensity profile of the IR pulse is displayed in Fig. 7(d). Both XUV and IR pulses are well reconstructed.

To test the quality of the reconstruction, we have calculated the percentage difference between the correct value of the pulse duration and the reconstructed one as a function of η. To study the effect of sparse sampling, we evaluated four different scenarios. We simulated spectrograms with relatively low ($D_2 = 7$ fs^2) or high ($D_2 = 20$ fs^2) XUV chirp (bandwidth unchanged), and with low or high IR peak intensity (corresponding to single or multiple sideband generation). The result is shown in Figs. 7(a)-(b) for XUV and IR pulses, respectively. The maximum value of the parameter η strongly depends on the GDD of the XUV pulses (transform-limited IR pulses were considered), while it is only weakly affected by IR intensity. In the case of low GDD (blue and red curves in Fig. 8), the reconstruction works well for $\eta < 1.3$, while for a relatively high GDD (light blue and orange curves in Fig. 8) the reconstruction is excellent for $\eta < 0.82$.
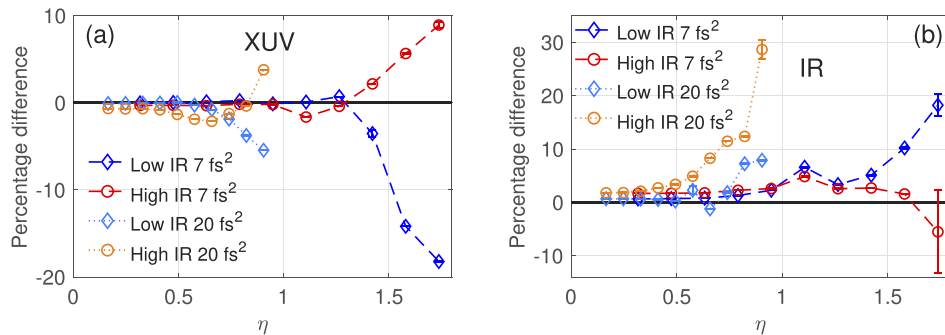

Fig. 8. Percentage difference between the correct value of the pulse duration and the reconstructed one as a function of η for the XUV (a) and IR (b) pulses. XUV pulses with two different GDD values were considered ($D_2 = 7$ fs^2 and $D_2 = 20$ fs^2). Low intensity: $I_{IR} = 1 \times 10^{11}$ W/cm^2; high intensity: $I_{IR} = 1 \times 10^{12}$ W/cm^2.

5. Effects of finite spectral resolution

So far we have considered pulse parameters leading to the generation of sidebands well separated from the spectrum of the main photoelectron peak (corresponding to the ionization induced only by the XUV pulse). Upon decreasing the pulse duration of the driving IR pulse and, consequently, of the XUV harmonic pulse, the sidebands start to spectrally overlap the main photoelectron peak, thus leading to the generation of an interference pattern. In this particular case, a limited spectral resolution of the electron spectrometer used for the acquisition of the photoelectron spectra may produce an excessive smoothing of the interference pattern, with a potential loss of

information about the temporal characteristics of the pulses. It is therefore interesting to analyse the effects of the experimental spectral resolution on pulse reconstruction.

Figure 9(a) shows the spectrogram calculated assuming a transform-limited IR pulse of 5-fs duration (FWHM) and an XUV pulse (H27) with a bandwidth corresponding to a transform-limited duration of 2 fs (FWHM) and a GDD $D_2 = 7$ fs^2, thus leading to a pulse duration of ~ 9.9 fs. Interference fringes are clearly visible around the zero delay. To mimic the experimental spectral resolution each photoelectron spectrum was then convoluted with a Gaussian response function with a FWHM-width of 200 meV. The result is shown in Fig. 9(b), where the interference pattern is barely visible. The reconstructed spectrogram is reported in Fig. 9(c). The solid blue and green curves in Fig. 9(d) correspond to the spectral amplitude and phase, respectively, of the XUV pulse. The blue and green circles represent the results of the reconstruction. Figure 9(e) shows the input (red solid curve) and the reconstructed (orange circles) temporal intensity profile of the IR pulse. The spectral and temporal characteristics of the XUV and IR pulses are well reconstructed, despite the not ideal spectral resolution. We remark that the ePIE reconstruction (Fig. 9(c)) is very similar to the spectrogram calculated without considering the finite spectral resolution of the experimental setup (Fig. 9(a)). This is a consequence of the fact that ePIE algorithm, as any FROG-CRAB algorithm, is based on a physical model, which is used to
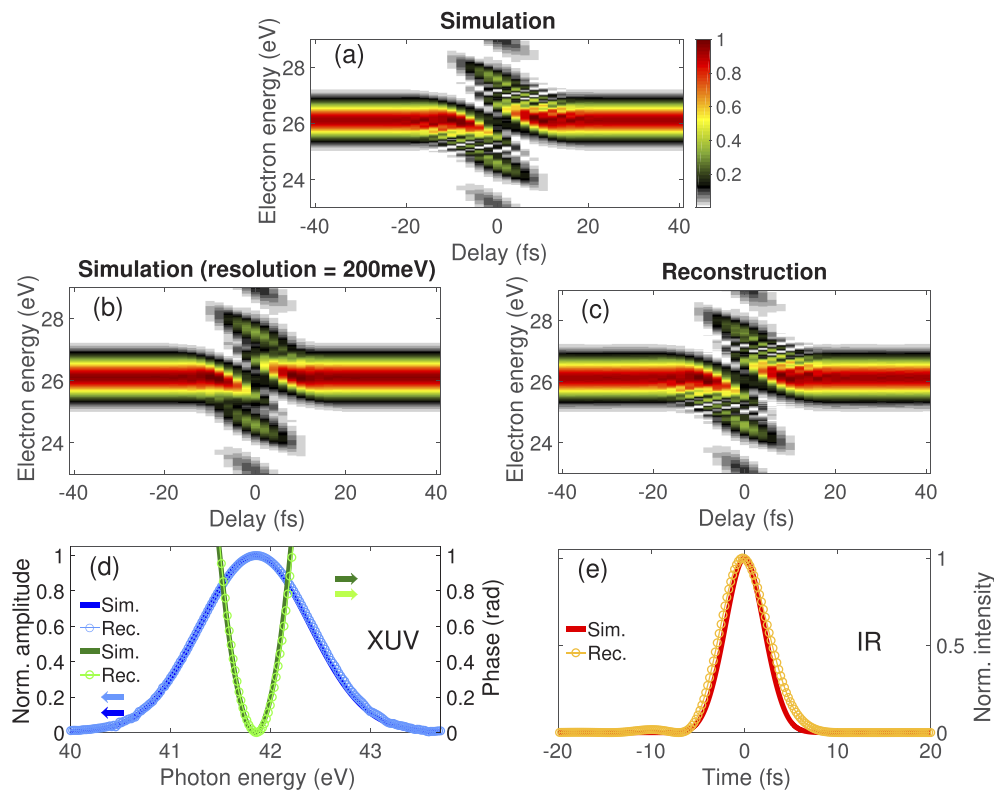

Fig. 9. Effects of finite spectral resolution on ePIE reconstruction for harmonic H27 assuming an XUV pulse with a bandwidth corresponding to a transform-limited duration of 2 fs (FWHM) and a GDD $D_2 = 7$ fs^2 (FWHM-duration $\Delta t_{XUV} = 9.9$ fs) and a 5-fs, transform-limited IR pulse with intensity $I_{IR} = 1 \times 10^{12}$ W/cm^2. (a) Simulated spectrogram; (b) simulated spectrogram considering a 200-meV spectral resolution; (c) reconstructed spectrogram; (d) simulated (solid lines) and reconstructed (circles) XUV spectral amplitude and phase; (e) simulated (solid line) and reconstructed (circles) IR temporal intensity profile.

calculate the spectrogram at each iteration. Therefore, the ePIE results will always be physical. On the contrary, the input matrix of this particular case (Fig. 9(b)) is not physical. Indeed, if two coherent electron wavepackets overlap in energy, interference fringes are produced. Since the ePIE approach necessarily converges towards the physical situation, such fringes will be correctly reproduced also in the case when the input spectrogram does not show them. This result, which is not common to all the reconstruction algorithms is another advantage of the ePIE approach.

Figures 10(a) and (b) display the calculated FWHM-duration of the XUV and IR pulses, respectively, as a function of the spectral resolution of the experimental setup (up to 200 meV) in the case of single- and multiple-sideband generation. The results are calculated considering a spectral resolution between 0 and 200 meV, thus corresponding to a relative energy resolution between 0% and 0.76%, since the mean kinetic energy of the photoelectrons generated by H27 is 26.09 eV. In the multiple-sideband regime, the XUV pulse duration is well reconstructed in the whole range of spectral resolution. In this case, there is a redundancy in the information that helps the convergence of the algorithm. When a single sideband is generated (low IR intensity regime) the reconstructed XUV duration clearly deviates from the correct value when the relative energy resolution is ∼ 0.57%. Moreover, in this case the standard deviation (error bars in Fig. 10) shows a clear dependence on spectral resolution. If the resolution is above ∼ 0.57% the reconstruction algorithm converges towards a wrong value of the XUV bandwidth. Depending on the temporal duration of the XUV pulse used as initial guess for the reconstruction, the algorithm converges towards longer or shorter durations. This observation is in good qualitative agreement with the results reported by Schweizer *et al.*, in the case of the application of time-domain ptychography to the reconstruction of self-amplification of spontaneous emission (SASE) X-ray pulses [26]. Also in this case, with an increasing relative energy resolution, the reconstruction error rapidly increased. Good reconstruction results were obtained with relative energy resolutions up to ∼ 0.35%.
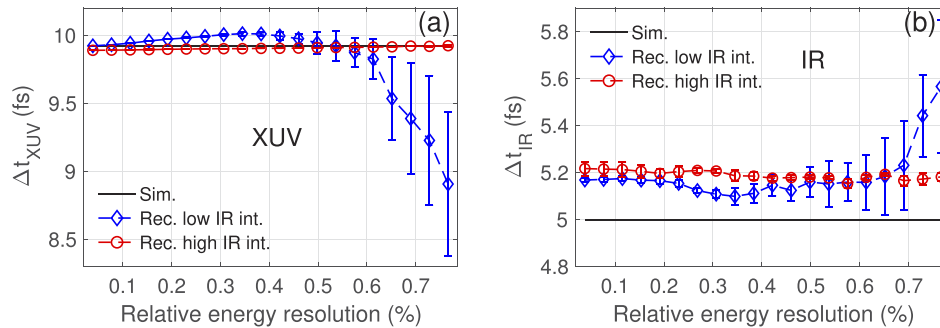

Fig. 10. Calculated FWHM-duration of the XUV (a) and IR (b) pulses as a function of the relative energy resolution of the experimental setup in the case of single- and multiple-sideband generation. Low intensity: $I_{IR} = 1 \times 10^{11}$ W/cm^2; high intensity: $I_{IR} = 1 \times 10^{12}$ W/cm^2.

6. Temporal characterization of low-photon-energy XUV pulses

In this section we will analyse the application of the ePIE approach to the reconstruction of XUV pulses with central photon energy close to the ionization potential of the gas used for the measurement of the FROG-CRAB spectrogram. In the following we will consider the 11-th harmonic (∼ 17 eV) measured using argon photo-ionization (I_p = 15.76 eV). In this case only the upper sidebands (i.e., the sidebands with photoelectron energy above $\hbar\omega_{H11} - I_p$) can be generated.

Also here we have analysed the robustness of ePIE reconstruction of both XUV and IR pulses for single- and multiple-sideband generation considering chirped XUV pulses. When a single sideband is generated, the ePIE reconstruction of the XUV pulse strongly depends on the initial guess on the XUV pulse duration. This is shown in Fig. 11 (blue diamonds), which displays the percentage difference between the correct value of the XUV pulse duration and the reconstructed
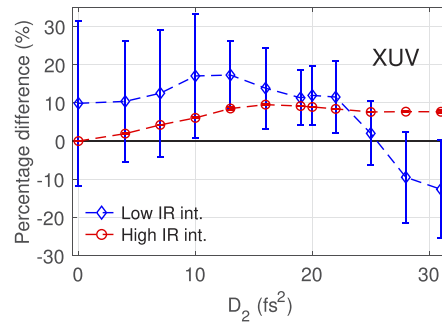

Fig. 11. Percentage difference between the correct value of the XUV pulse duration and the reconstructed one as a function of the GDD of the XUV pulses (with a bandwidth-limited duration of 5 fs), in the case of harmonic H11 assuming a transform-limited, 10-fs, IR pulse with intensity $I_{IR} = 1 \times 10^{11}$ W/cm^2 (blue diamonds: low intensity) and $I_{IR} = 1 \times 10^{12}$ W/cm^2 (red circles: high intensity).
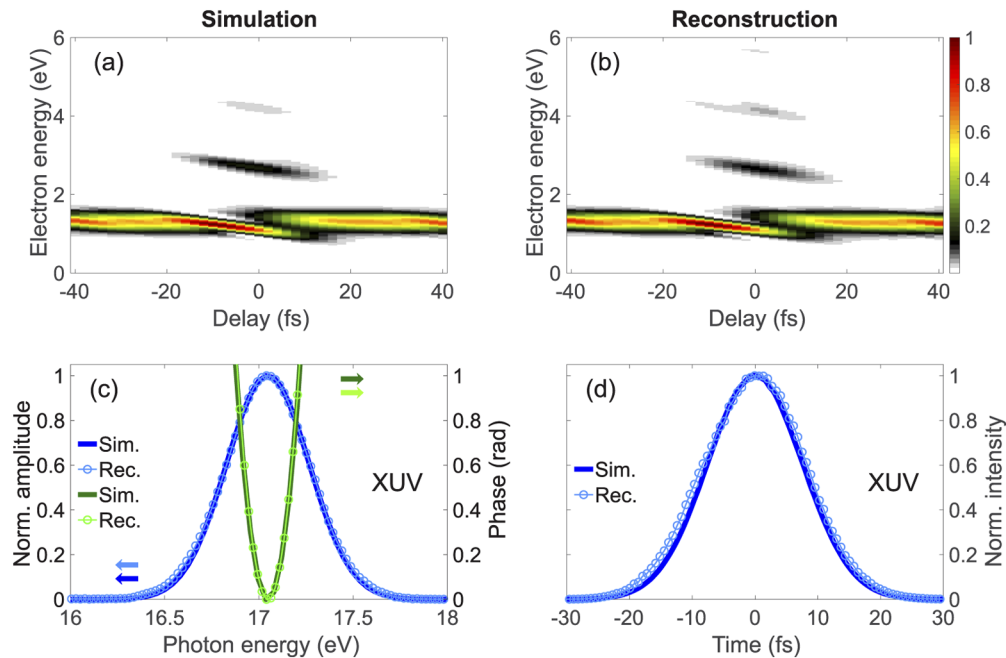

Fig. 12. Temporal characterization of low-photon-energy XUV pulses in the case of harmonic H11 assuming a chirped XUV pulse, with bandwidth-limited duration of 5 fs and $D_2 = 31$ fs^2 (FWHM-duration $\Delta t_{XUV} = 17.9$ fs) and a transform-limited, 10-fs, IR pulse with intensity $I_{IR} = 4 \times 10^{12}$ W/cm^2. Simulated (a) and reconstructed (b) spectrograms. (c) Simulated (solid lines) and reconstructed (circles) XUV spectral amplitude and phase. (d) Simulated (solid line) and reconstructed (circles) XUV intensity temporal profile.

one as a function of the GDD of the XUV pulses. The error bars, calculated considering different initial guesses for the XUV pulse duration, are very large even in the case of transform-limited pulses. Moreover, the temporal characteristics of the IR pulse are typically not accurately reproduced.

In the case of multiple-sideband generation, while the IR pulse is still not well reconstructed, the ePIE reconstruction of the XUV pulse does not appreciably depend on the initial guess on XUV pulse duration, as shown by the very small error bars in Fig. 11 (red circles). The percentage difference between the correct value of the XUV pulse duration and the reconstructed one is <10% even in the case of large GDD. As an example, we report in Fig. 12 the simulation and reconstruction results in case of a strongly chirped XUV pulse (H11) (D_2 = 31 fs^2, giving a FWHM-pulse duration Δt_{XUV} = 17.9 fs) and high IR intensity: the spectral and temporal characteristics of the XUV pulse are nicely reconstructed.

7. Reconstruction of non-Gaussian pulses

So far we always assumed Gaussian IR and XUV pulses. To test the goodness of the ePIE algorithm to correctly reconstruct pulses in a more general case, we performed simulations with realistic pulses. The procedure we adopted is the following. We measured the temporal characteristics of an IR pulse at the output of an hollow-fiber pulse compressor [27] by using the second harmonic generation FROG (SHG-FROG) technique. The reconstructed pulse intensity profile is shown by the red solid line in Fig. 13(d). The pulse, with a FWHM duration of 10.2 fs, is asymmetric, with small wings extending from ∼ −30 fs to ∼ 30 fs. By using the nonadiabatic saddle-point method [28], the high-order harmonic spectrum generated by the measured IR pulse was calculated. We then selected the 27-th harmonic in the simulated harmonic spectrum, preserving its intrinsic spectral phase. Being H27 in the cut-off region of the simulated spectrum,
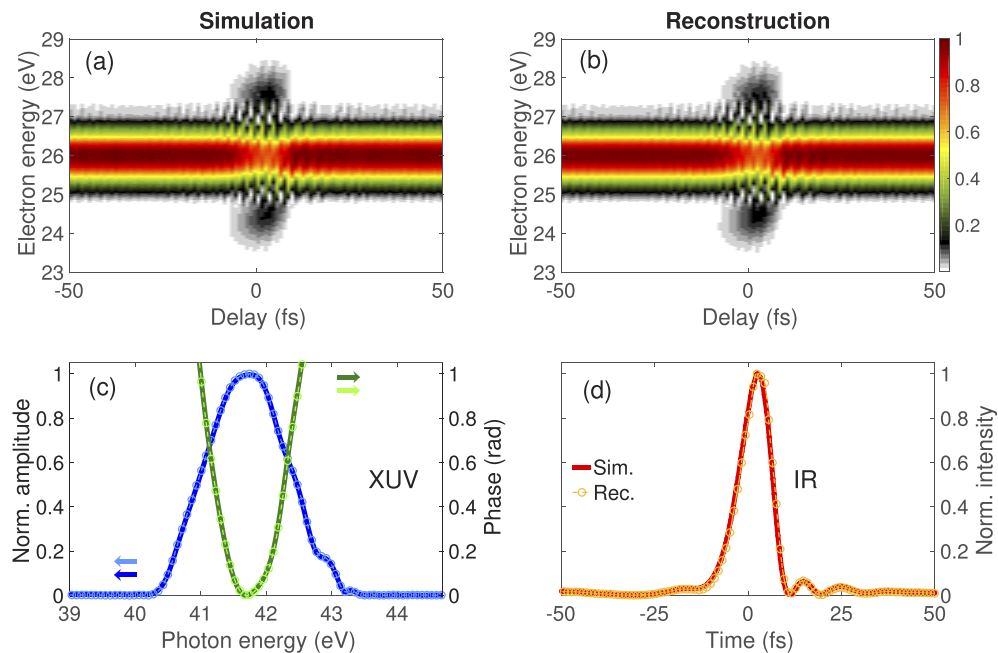

Fig. 13. Reconstruction of non-Gaussian pulses. Simulated (a) and reconstructed (b) spectrograms. (c) Simulated (solid lines) and reconstructed (circles) XUV spectral amplitude and phase. (d) Simulated (solid line) and reconstructed (circles) IR temporal intensity profile.

it has a non-symmetric temporal profile. The FWHM duration is about 3-4 fs. For the sake of simplicity, we did not introduce the temporal dispersion of the TDCM. We used this H27 and the generating field (with properly rescaled peak intensity), to calculate the spectrogram shown in Fig. 13(a). Finally, we used ePIE to reconstruct the spectrogram (the reconstructed spectrogram is displayed in Fig. 13(b)) and compare the retrieved pulses with the inputs. We found excellent agreement for both low (1×10^{11} W/cm^2) and high (1×10^{12} W/cm^2, not reported in Fig. 13) IR intensities. We observed that the presence of multiple sidebands helps the algorithm to reach faster convergence in this case.

8. Conclusions

We have demonstrated, by using numerical simulations, that the extended ptychographic iterative engine (ePIE) algorithm is a particularly robust reconstruction technique for the inversion of FROG-CRAB spectrograms produced by few-femtosecond XUV pulses. The spectral and temporal characteristics of these pulses can be measured even in presence of various experimental limitations: jitter of the relative delay between XUV and IR pulses, reduced signal-to-noise ratio, reduced number of measured time delays, low spectral resolution of the experimental apparatus used for the measurement, incomplete generation of the sideband pattern (low photoelectron kinetic energy). Various experimental criteria to achieve a good pulse reconstruction have been identified, which depend on the XUV pulse characteristics (in particular, duration and chirp) and on the particular experimental limitations mainly affecting the measurement. We found that the generation of spectrograms with multiple sidebands, obtained by increasing the intensity of the IR pulse, is advantageous in the case of poor signal-to-noise ratio of the measurement, in the presence of a limited spectral resolution of the experimental apparatus and when XUV pulses with central energy close to the ionization potential of the chosen target gas must be characterised.

Disclosures

The authors declare no conflicts of interest.

References

1. B. Erk, R. Boll, S. Trippel, D. Anielski, L. Foucar, B. Rudek, S. W. Epp, R. Coffee, S. Carron, S. Schorb, K. R. Ferguson, M. Swiggers, J. D. Bozek, M. Simon, T. Marchenko, J. Küpper, I. Schlichting, J. Ullrich, C. Bostedt, D. Rolles, and A. Rudenko, "Imaging charge transfer in iodomethane upon x-ray photoabsorption," Science **345**(6194), 288–291 (2014).
2. J. Schnadt, P. A. Brühwiler, L. Patthey, J. N. O'Shea, S. Sodergren, M. Odelius, R. Ahuja, O. Karis, M. Bassler, P. Persson, H. Siegbahn, S. Lunell, and N. Martensson, "Experimental evidence for sub-3-fs charge transfer from an aromatic adsorbate to a semiconductor," Nature **418**(6898), 620–623 (2002).
3. A. Ludwig, E. Liberatore, J. Herrmann, L. Kasmi, P. López-Tarifa, L. Gallmann, U. Rothlisberger, U. Keller, and M. Lucchini, "Ultrafast Relaxation Dynamics of the Ethylene Cation $C_2H_4^+$," J. Phys. Chem. Lett. **7**(10), 1901–1906 (2016).
4. M. Eckstein, C. Yang, M. Kubin, F. Frassetto, L. Poletto, H. Ritze, M. J. J. Vrakking, and O. Kornilov, "Dynamics of N_2 Dissociation upon Inner-Valence Ionization by Wavelength-Selected XUV Pulses," J. Phys. Chem. Lett. **6**(3), 419–425 (2015).
5. M. Nisoli, P. Decleva, F. Calegari, A. Palacios, and F. Martín, "Attosecond electron dynamics in molecules," Chem. Rev. **117**(16), 10760–10825 (2017).
6. L. Poletto and P. Villoresi, "Time-delay-compensated monochromator in the off-plane mount for extreme-ultraviolet ultrashort pulses," Appl. Opt. **45**(34), 8577–8585 (2006).
7. L. Poletto, P. Villoresi, E. Benedetti, F. Ferrari, S. Stagira, G. Sansone, and M. Nisoli, "Intense femtosecond extreme ultraviolet pulses by using a time-delay-compensated monochromator," Opt. Lett. **32**(19), 2897–2899 (2007).
8. L. Poletto, P. Villoresi, E. Benedetti, F. Ferrari, S. Stagira, G. Sansone, and M. Nisoli, "Temporal characterization of a time-compensated monochromator for high-efficiency selection of XUV pulses generated by high-order harmonics," J. Opt. Soc. Am. B **25**(7), B44–B49 (2008).
9. L. Poletto, P. Villoresi, F. Frassetto, F. Calegari, F. Ferrari, M. Lucchini, G. Sansone, and M. Nisoli, "Time-delay compensated monochromator for the spectral selection of extreme-ultraviolet high-order laser harmonics," Rev. Sci. Instrum. **80**(12), 123109 (2009).

10. M. Lucchini, G. Lucarelli, M. Murari, A. Trabattoni, N. Fabris, F. Frassetto, S. De Silvestri, L. Poletto, and M. Nisoli, "Few-femtosecond extreme-ultraviolet pulses fully reconstructed by a ptychographic technique," Opt. Express **26**(6), 6771–6784 (2018).
11. Y. Mairesse and F. Quéré, "Frequency-resolved optical gating for complete reconstruction of attosecond bursts," Phys. Rev. A **71**(1), 011401 (2005).
12. G. Sansone, E. Benedetti, F. Calegari, C. Vozzi, L. Avaldi, R. Flammini, L. Poletto, P. Villoresi, C. Altucci, R. Velotta, S. Stagira, S. De Silvestri, and M. Nisoli, "Isolated Single-Cycle Attosecond Pulses," Science **314**(5798), 443–446 (2006).
13. J. Gagnon, E. Goulielmakis, and V. S. Yakovlev, "The accurate FROG characterization of attosecond pulses from streaking measurements," Appl. Phys. B **92**(1), 25–32 (2008).
14. J. Itatani, F. Quéré, G. L. Yudin, M. Y. Ivanov, F. Krausz, and P. B. Corkum, "Attosecond Streak Camera," Phys. Rev. Lett. **88**(17), 173903 (2002).
15. D. Spangenberg, E. Rohwer, M. H. Brügmann, and T. Feurer, "Ptychographic ultrafast pulse reconstruction," Opt. Lett. **40**(6), 1002–1005 (2015).
16. M. Lucchini, M. H. Brügmann, A. Ludwig, L. Gallmann, U. Keller, and T. Feurer, "Ptychographic reconstruction of attosecond pulses," Opt. Express **23**(23), 29502–29513 (2015).
17. P. Sidorenko, O. Lahav, Z. Avnat, and O. Cohen, "Ptychographic reconstruction algorithm for frequency-resolved optical gating: super-resolution and supreme robustness," Optica **3**(12), 1320–1330 (2016).
18. J. M. Rodenburg, "Ptychography and related diffractive imaging methods," Adv. Imaging Electron Phys. **150**, 87–184 (2008).
19. D. Spangenberg, P. Neethling, E. Rohwer, M. H. Brügmann, and T. Feurer, "Time-domain ptychography," Phys. Rev. A **91**(2), 021803 (2015).
20. M. Kitzler, N. Milosevic, A. Scrinzi, F. Krausz, and T. Brabec, "Quantum theory of attosecond XUV pulse measurement by laser dressed photoionization," Phys. Rev. Lett. **88**(17), 173904 (2002).
21. M. Rhodes, G. Steinmeyer, J. Ratner, and R. Trebino, "Pulse-shape instabilities and their measurement," Laser Photonics Rev. **7**(4), 557–565 (2013).
22. E. Escoto, R. Jafari, R. Trebino, and G. Steinmeyer, "Retrieving the coherent artifact in frequency-resolved optical gating," Opt. Lett. **44**(12), 3142–3145 (2019).
23. C. Bourassin-Bouchet and M.-E. Couprie, "Partially coherent ultrafast spectrography," Nat. Commun. **6**(1), 6465 (2015).
24. M. Lucchini and M. Nisoli, "Refined Ptychographic Reconstruction of Attosecond Pulses," Appl. Sci. **8**(12), 2563 (2018).
25. K. W. DeLong, D. N. Fittinghoff, and R. Trebino, "Practical issues in ultrashort-laser-pulse measurement using frequency-resolved optical gating," IEEE J. Quantum Electron. **32**(7), 1253–1264 (1996).
26. T. Schweizer, M. H. Brügmann, W. Helml, N. Hartmann, R. Coffee, and T. Feurer, "Attoclock Ptychography," Appl. Sci. **8**(7), 1039 (2018).
27. M. Nisoli, S. De Silvestri, and O. Svelto, "Generation of high energy 10 fs pulses by a new pulse compression technique," Appl. Phys. Lett. **68**(20), 2793–2795 (1996).
28. M. Lucchini, F. Calegari, K. Kim, G. Sansone, and M. Nisoli, "Nonadiabatic quantum path analysis of high-order harmonic generation in a highly ionized medium," New J. Phys. **14**(3), 033009 (2012).